A Novel Spectral-Spatial Singular Spectrum Analysis Technique for Near Real-Time *In Situ* Feature Extraction in Hyperspectral Imaging

Hang Fu, Genyun Sun, *Member, IEEE*, Jaime Zabalza, *Member, IEEE*, Aizhu Zhang, *Member, IEEE*, Jinchang Ren, *Senior Member, IEEE*, and Xiuping Jia, *Senior Member, IEEE*

***Abstract*—As a cutting-edge technique for denoising and feature extraction, singular spectrum analysis (SSA) has been applied successfully for feature mining in hyperspectral images (HSI). However, when applying SSA for *in situ* feature extraction in HSI, conventional pixel-based 1-D SSA fails to produce satisfactory results, while the band-image-based 2D-SSA is also infeasible especially for the popularly used line-scan mode. To tackle these challenges, in this article, a novel 1.5D-SSA approach is proposed for *in situ* spectral-spatial feature extraction in HSI, where pixels from a small window are used as spatial information. For each sequentially acquired pixel, similar pixels are located from a window centered at the pixel to form an extended trajectory matrix for feature extraction. Classification results on two well-known benchmark HSI datasets and an actual urban scene dataset have demonstrated that the proposed 1.5D-SSA achieves the superior performance compared with several state-of-the-art spectral and spatial methods. In addition, the near real-time implementation in aligning to the HSI acquisition process can meet the requirement of online image analysis for more efficient feature extraction than the conventional offline workflow.**

***Index Terms*—Feature extraction, hyperspectral image (HSI), near real-time, singular spectrum analysis (SSA), spectral-spatial.**

I. Introduction

THE rapid development of the modern sensors and computing technologies has put forward increasing demanding for the effective and efficient analysis and interpretation of digital images. In the electronics field, image processing and machine vision techniques can help to interpret and analyze the target images according to specific requirements. Therefore, these have been widely used in many application fields, such as medical, remote sensing, transportation, and military.

In recent years, some novel and effective image processing techniques have been proposed for different machine vision applications. For instance, an efficient Cellular Learning Automata (CLA) has been used in channel assignment in cellular networks and call admission control [1], image steganography [2], and image encryption [3]. For real-time pedestrian detection, a five-stage DSWTS technique is proposed to overcome the shortcomings in the application of machine vision to identify pedestrians, using a single CMOS camera [4]. In the remote sensing domain, two statistics-based feature extraction methods, the kurtosis wavelet energy (KWE), and the kurtosis curvelet energy (KCE), have been used in SAR images as well as medical images, which have been applied for effectively texture recognition and image segmentation [5], [6]. In coastline detection, some techniques are proposed to improve the detection accuracy combining certain image features and mathematical approach, based on different satellite data such as Sentinel-1 [7] and multispectral images [8]. In [9], an improved parameter-free method is used for Polarimetric Synthetic Aperture Radar image segmentation, which can improve both the performance and the noise resistance compared with conventional methods.

In remote sensing image processing, feature extraction and mining is of high importance for image analysis, especially for hyperspectral image (HSI). Hyperspectral remote sensing is an application based on the acquisition of multidimensional information combining spatial and spectral content, thanks to hyperspectral devices such as the Airborne Visible/Infrared Imaging Spectrometer [10]. Compared with full-color and multispectral remote sensing images, HSI contains rich spectral information, which is related to the physical nature of the materials and can be used to detect minor object differences in terms of moisture, temperature, and chemical components [11]. However, due to the intrinsic nature of HSI data, redundancy and noise are unavoidable during data acquisition, transmission, and processing, which limits the benefits of the HSI technology [12], [13].

In order to overcome these shortcomings, efforts such as the extraction of more effective features in both spatial and spectral domains are suggested [14]. Some widely used spectral feature extraction techniques such as the principal component analysis (PCA) [11], [15] and singular spectrum analysis (SSA) [16], [17]

Manuscript received December 20, 2019; revised March 16, 2020 and April 24, 2020; accepted April 26, 2020. Date of publication May 14, 2020; date of current version May 29, 2020. This work was supported by the National Natural Science Foundation of China under Grant 41971292, Grant 41801275, and Grant 41871270. *(Corresponding author: Genyun Sun.)*

Hang Fu, Genyun Sun, and Aizhu Zhang are with the College of Oceanography and Space Informatics, China University of Petroleum (East China), Qingdao 266580, China, and also with the Laboratory for Marine Mineral Resources, Qingdao National Laboratory for Marine Science and Technology, Qingdao 266237, China (e-mail: hangf_upc@163.com; genyunsun@163.com; zhangaizhu789@163.com).

Jaime Zabalza and Jinchang Ren are with the Department of Electronic and Electrical Engineering, University of Strathclyde, G11XW Glasgow, U.K. (e-mail: jinchang.ren@strath.ac.uk).

Xiuping Jia is with the School of Engineering and Information Technology, University of New South Wales at Canberra, Canberra, ACT 2600, Australia (e-mail: x-jia@adfa.edu.au).

Digital Object Identifier 10.1109/JSTARS.2020.2992230

can obtain effective spectral features in the transform domain. SSA has demonstrated a good ability and effectiveness to extract signal trend and remove high-frequency noise in HSI pixels, but it ignores the spatial information from the hyperspectral cubes. Because of the limitation of spectral feature extraction, as well as the potential use of spatial information, some spatial processing techniques have been proposed. One popular approach for spatial feature extraction is based on the morphological profile (MP), such as the extended attribute profiles (EAP) [18]. Gabor features can represent spatial structures of different scales and orientations in HSI [19]. The 2-D version of SSA (2D-SSA) [20], [21] extract global spatial information for each band image, but it could oversmooth the data and lead to a classification error. In addition, there are some techniques that utilize spectral-spatial information, such as edge-preserving filters (EPF) based methods [22], intrinsic image decomposition [23], extended random walker [24], while belonging to shallow structural models.

Recently, deep learning has become a hot research topic in image processing and is utilized for various applications, such as change detection [25], image classification [26], [27], and image segmentation [28]. With the network architectures, deep learning techniques can extract deeper level and more abstract features of the data, achieving more promising performance than traditional models with shallower structures [29], [30]. Deep convolutional neural networks (CNN) based methods usually outperform other deep learning models due to its unique and useful characteristics. CNN and its modifications have been widely used for HSI spectral-spatial classification [31], [32], and it can further combine with other techniques, such as MP [33] and sparse representation [34] to improve the classification performance. However, deep learning methods have numerous training parameters and are mostly introduced as a black box. For HSI applications, conventional approaches are still desirable due to mainly the lack of insufficient training samples for training the deep learning models.

Furthermore, due to the high dimensionality of HSI and the large computational complexity of processing algorithms, developing fast image processing techniques has become a popular research area. Previous research works, such as real-time PCA [35], near real-time endmember [36], and real-time target detection [37] have proposed different fast hyperspectral processing techniques for various applications, based on the feature extraction. Moreover, there are also some fast implementation techniques proposed in the recent literature. In [38], the real-time technique is applied for the detection of desired targets, which can process pushbroom data on-the-fly, reducing the amount of data to be stored and processed on-board. In [39], a low-power-consumption but lossy compression solution is presented for real-time hyperspectral imaging on-board compression, mainly oriented to the application of smart farming. These online processing techniques can effectively improve the efficiency.

In this article, a novel near real-time feature extraction strategy based on the SSA method is introduced, combining with the scanning manner of hyperspectral. This method can utilize the local spatial-spectral feature of captured pixels, and is called 1.5D-SSA mainly because its processing mode is between SSA and 2D-SSA. Unlike conventional SSA, the proposed method is locally applied to small regions (defined by central pixel and its neighborhood pixels), considering not only the rich spectral information but also the local spatial content. In addition, we applied this method for captured pixels in a local window during the imaging process of HSI, so that pixels can be processed online. However, it starts processing only if the captured pixels are enough to form a small local region, thus it is a near real-time mode. Compared with postprocessing methods, this method can reduce the associated computational costs.

The rest of this article is organized as follows: The following section introduces the related works. Our proposed method is presented in Section III. Section IV assesses the performance of the processing strategy through experimental analysis. Finally, Section V concludes this article.

II. Related Works

This section is divided into two parts: First, two of the most common acquisition paradigms in HSI are briefly explained, as the real-time processing of the approach proposed in this article is based on these paradigms. Second, the implementation of the conventional SSA is recalled. This SSA implementation is for performing feature extraction exclusively in the spectral domain, but its principles are used in the proposed strategy.

A. Data Acquisition in HSI

Hyperspectral cubes in HSI present two spatial dimensions along with a high-resolution spectral dimension. Therefore, HSI acquisition requires scanning in the spectral or spatial domains [40]. As a sequential data collection procedure, the scanning techniques or paradigms obtain partial scenes in the spatial domain along with their corresponding spectra to construct the final image cube.

The two most common paradigms in scanning techniques may be the whisk-broom and the push-broom scanning [35], [41]. The whisk-broom scanning (also known as pixel scanning) acquires HSI data pixelwise, while the push-broom scanning (also known as line scanning), is able to collect several pixels forming a row (or a column) in the spatial scene at the same time. The proposed approaches can be easily implemented in parallel with the two paradigms.

B. Conventional SSA

For a given 1-D signal $x = [x_1, x_2, \ldots, x_N] \in R^N$ and an embedding window of size L, the original signal can be mapped into a sequence of lagged vectors, i.e., the trajectory matrix X. The matrix X has equal values along the antidiagonals, which forms a Hankel matrix by definition.

Let us denote the Eigenvalues of XX^T and their corresponding Eigenvectors as $(\lambda_1 \geq \lambda_2 \geq \cdots \geq \lambda_L)$ and $(U_1, U_2, \ldots, U_L)$, respectively. The trajectory matrix can be reconstructed as the sum of several elementary matrices as follows:

$$X = X_1 + X_2 + \cdots + X_L$$
$$(X_i = \sqrt{\lambda_i} U_i {V_i}^T, V_i = X^T U_i / \sqrt{\lambda_i}) \quad (1)$$

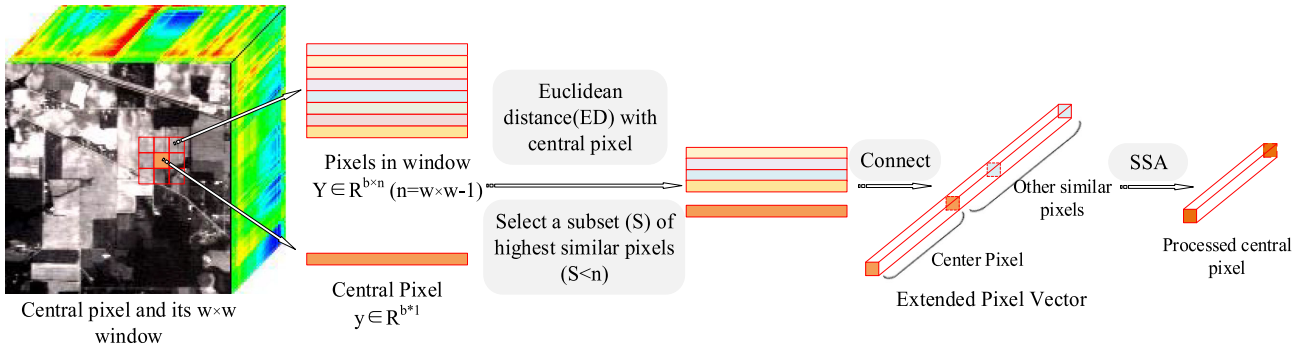

Fig. 1. Flowchart of the proposed 1.5D-SSA method.

where U_i and V_i are the empirical orthogonal functions and the principal components (PC) of the ith elementary matrix of the trajectory matrix, respectively. After Eigenvalue grouping (EVG), a subset of X_i is selected as an approximation to the trajectory matrix X, which contains the main trend component and eliminates the noise component.

The resulting matrices obtained by grouping are unnecessarily the Hankel type matrix as the original trajectory matrix is. A diagonal averaging is needed to average the antidiagonal values in the matrix and project the matrices into the new 1-D signals, a process known as Hankelisation as detailed in [42].

As suggested in [16] and [17], in most cases the first component that corresponds to the maximum Eigenvalue can sufficiently represent the original pixel. Therefore, in our experiments (see Section IV), the SSA parameter for EVG is fixed to 1. To this end, the window size L becomes the only parameter for configuring the conventional SSA.

III. Proposed Methodology

In this section, the novel 1.5D-SSA for near real-time processing is introduced. This methodology can be easily explained in two different parts: First, 1.5D-SSA is developed, where conventional SSA is applied to a vector made of the concatenation of several pixels from local spatial neighborhoods in the image. Second, the implementation of this 1.5D-SSA is adapted for (near) real-time processing, according to two of the most common acquisition paradigms in HSI, i.e., pixel scanning and line scanning.

A. 1.5D-SSA

The conventional SSA method for the HSI data feature extraction is applied on each pixel vector and exploits the spectral content yet ignores any spatial information. For an efficient use of spectral and local spatial information, the proposed 1.5D-SSA method works in local spatial regions and uses the similarity information from neighboring pixels. A schematic flowchart is illustrated in Fig. 1.

As shown in Fig. 1, for each pixel, a small neighborhood window ($w \times w$) is selected from which pixels with highest similarity to the central one are used to construct an extended vector. The similarity measurement used here is the Euclidean distance (ED). A subset (S) of highest similar pixels is selected and sorted according to their ED values. Next, the central pixel and the selected ones are arranged as 1-D vector following the ED values order (smaller EDs go first), i.e., pixels with higher similarity are closer to the central pixel. The pixels in window which have the same ED values can be random arrangement. Finally, conventional SSA is applied to this extended vector, where those values in the vector range corresponding to the central pixel are extracted as outcome. Applying this to all the pixels, the original hypercube can be transformed to a new hypercube with 1.5D-SSA pixels.

Compared to spectral pixel vector, the extended vector can construct a new extend Hankel matrix, where the lagged vectors contain not only continuous spectral information but also spatial information of adjacent pixels. Such information is also added to the covariance matrix in the SVD stage, the reconstructed matrix subset can better represent the local features of the center pixel, in other words, the spectral features and local similarity features are concentrated on the central given pixel. Therefore, this method combining Spectral and spatial information is expected to provide better feature extraction and classification performance in HSI.

B. Near Real-Time Processing for 1.5D-SSA

According to the aforementioned proposed method, the algorithm needs a local small neighborhood for each pixel under processing to perform 1.5D-SSA. Therefore, when the number of acquired pixels by the HSI device is enough to form a small neighborhood (depends on the window size), the proposed method starts to process the related central pixel. Due to the difference in time between the pixel being acquired and the pixel being processed, this processing can be considered near real time. Fig. 2 demonstrates the processing flow of 1.5D-SSA during HSI acquisition with a small neighborhood of 3×3.

Fig. 2 shows two processing flows for 1.5D-SSA corresponding to pixel scanning and line scanning, respectively. For pixel scanning, the HSI device collects a pixel at a time and the proposed method starts processing a given pixel when there are enough pixels to form, in this example, a 3×3 neighborhood. Both pixel acquisition and pixel processing directions are the same, with a fixed time lag between them. For line scanning,

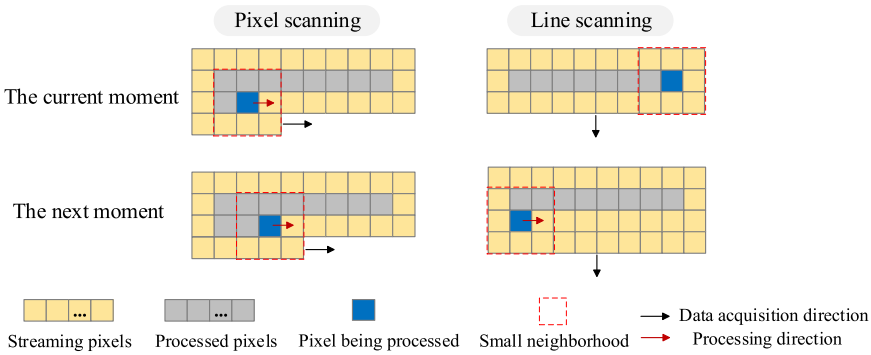

Fig. 2. Processing flow of 1.5D-SSA (3 × 3 window) during different HSI acquisition scanning techniques.

one row (or column) of pixels is collected at a time, and after collection of, in this case three rows, the proposed method begins to process a given pixel. In the line scanning paradigm, the speed of pixel acquisition is faster than that of pixel processing, and the time difference between acquisition and processing increases gradually.

Note that in both pixel and line scanning, the edge pixels of the images have not been processed during the collection process, because the edge pixels have not neighborhood pixels to form windows. These pixels can be processed separately by SSA or 1.5D-SSA with pixel supplement after the completion of collection. In addition, these pixels are also can be neglected as the window size is too small compared with image size.

IV. Experiments and Results

In this section, the effectiveness in feature extraction and noise reduction of the proposed method is validated using two benchmark HSI datasets, as well as one actual HSI dataset, in a number of experiments, presenting results that demonstrate the related benefits in the HSI pixel classification.

A. HSI Datasets and Experimental Settings

Two benchmark HSI datasets with available ground truth, Indian Pines and Pavia University, are used in the experiments. The Indian Pines dataset has a spatial size of 145 × 145 pixels containing 220 contiguous spectral bands (normally reduced to 200 to avoid noisy and water absorption bands) with a wavelength range going from 400 to 2500 nm and including 16 land-cover classes in the ground truth. The second dataset, Pavia University, has a spatial size of 610 × 340 pixels and 115 spectral bands (reduced to 103) across a range from 430 to 860 nm, with nine land-cover classes.

In addition, another actual HSI dataset, DFC2018 Houston, is added in our experiment. This dataset was from 2018 IEEE GRSS Data Fusion Contest, a real urban scene for classification.[1] The dataset was acquired by the National Center for Airborne Laser Mapping) sensor over the University of Houston campus and its neighboring areas on Feb. 16, 2017 between 16:31 and 18:18 GMT, covering a spectral range of 380–1050 nm with 48 bands at a 1-m Ground Sample Distance. Considering the efficiency and computational complexity, a subscene of 1000 × 1000 pixels is used in our experiment, which contains 12 land-cover classes in the associated ground-truth map.

HSI pixels classification is performed to evaluate the efficacy of the proposed feature extraction method, as enhanced features are expected to lead to higher classification accuracies. Support vector machine (SVM) is usually selected as classifier in the related literature, mainly because it presents high robustness to the Hughes phenomenon [43], [44]. The SVM classifier is implemented by the LIBSVM library [45], using a Gaussian kernel with a fivefold cross validation. In order to train SVM models, 10% randomly selected samples per class are taken as training set, being the rest of samples used for testing. Three commonly used performance metrics are utilized to evaluate the proposed method: overall accuracy (OA), average accuracy, and kappa coefficient, from classification tasks.

The different ground truth classes and the number of training samples in each class for the two datasets are listed in Tables I–III, respectively.

B. Parameters Analysis

The proposed 1.5D-SSA method is configured by three parameters. These are the neighborhood window size ($w \times w$), the embedding window L, and the number of similar pixels S used to construct the extended vector. The effect of these parameters in the HSI classification accuracies for both datasets are shown in Fig. 3.

The embedding window L determines joint spectral-spatial content of lagged vectors in trajectory matrix, as well as the degree of decomposition. An appropriate L can effectively separate useful spectral information from noisy content. The experimental results show that a value of $L = 20$ seems to provide the best performance, with smaller values leading to worse classification accuracy, while larger values are not able to improve it.

In addition, the two parameters, w and S together determine the degree of extraction and use of similar information related to the central pixel. The appropriate local region contains some spectrally similar pixels [14], [46], which can provide some spatial information, beneficial to the performance of our method. The undertaken analysis demonstrates that window size is 5 × 5

[1]Online. [Available]: check http://hyperspectral.ee.uh.edu/?page_id=1075

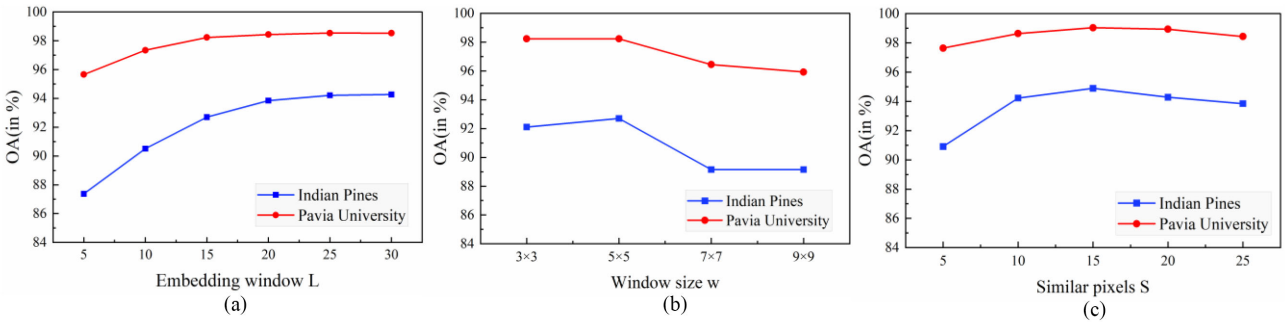

Fig. 3. Effect of the three configuration parameters of the proposed method in the classification OA for Indian Pines and Pavia University datasets. The fixed parameters are (a) 5×5 and $S = 25$, (b) $L = 15$, $S = w \times w$, and (c) 5×5 and $L = 20$, respectively.

TABLE I
INDIAN PINES DATASET INFORMATION

No.	Class description	Number of Samples
C1	Alfalfa	46
C2	Corn-notill	1428
C3	Corn-mintill	830
C4	Corn	237
C5	Grass-pasture	483
C6	Grass-trees	730
C7	Grass-pasture-mowed	28
C8	Hay-windrowed	478
C9	Oats	20
C10	Soybean-notill	972
C11	Soybean-mintill	2455
C12	Soybean-clean	593
C13	Wheat	205
C14	Woods	1265
C15	Buildings	386
C16	Stone-Steel-Towers	93

TABLE II
PAVIA UNIVERSITY DATASET INFORMATION

No.	Class description	Number of Samples
C1	Asphalt	6631
C2	Meadows	18649
C3	Gravel	2099
C4	Trees	3064
C5	Painted metal sheets	1345
C6	Bare Soil	5029
C7	Bitumen	1330
C8	Self-Blocking Bricks	3682
C9	Shadows	947

TABLE III
DFC2018 HOUSTON DATASET INFORMATION

No.	Class description	Number of Samples
C1	Healthy grass	812
C2	Stressed grass	15388
C3	Evergreen trees	5523
C4	Deciduous trees	1146
C5	Residential buildings	97864
C6	Non-residential buildings	69446
C7	Roads	52282
C8	Sidewalks	1958
C9	Major thoroughfares	62910
C10	Paved parking lots	4222
C11	Unpaved parking lots	587
C12	Cars	733

and $S = 15$ lead to the best results. Note that the parameters analysis implements based on two benchmark HSI datasets, and the obtained optimal parameters also achieve the best performance on the actual dataset by postvalidation.

C. Results in Feature Extraction and Denoising

Similar to SSA, the proposed 1.5D-SSA can extract main trend of the target pixel while suppressing the noisy content, but the preserved spectral features are different. In Fig. 4, an original pixel from the Indian Pines dataset as example is shown and compared with the reconstructed versions using conventional SSA ($L = 10$ and 20) and proposed 1.5D-SSA ($L = 10$), the EVG are all fixed at once.

As can be seen in Fig. 4, conventional SSA preserves only the general trend of the pixel and ignores the higher frequency peaks of the spectral profile. Therefore, conventional SSA can fail to preserve detailed information, which may be useful in distinguishing the spectra between different land-cover classes. Moreover, a strong smoothing effect may lead to the confusion of pixels corresponding to different land-cover classes. In contrast,

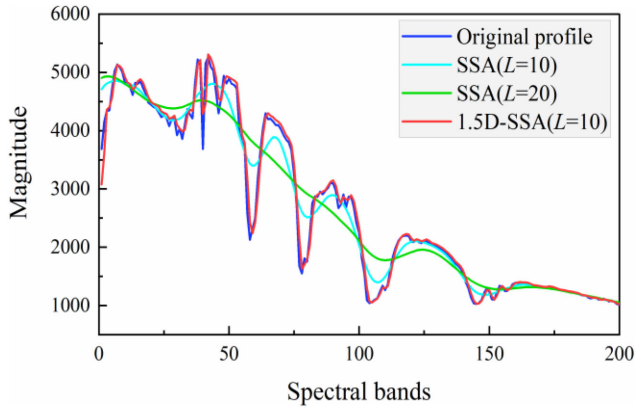

Fig. 4. Original and reconstructed pixel (by SSA and the proposed 1.5D-SSA, respectively) from the Indian Pines dataset.

the proposed method is able to avoid these problems, as it can smooth the fluctuation of spectral curves at a higher frequency peaks, eliminating the influence of noise and extracting improved spectral features.

D. Results in Classification

In this section, the classification results of the proposed method on two datasets are evaluated and compared with the raw data and seven other features extracted from the PCA, conventional SSA, EAP, Gabor filtering, EPF, and two deep learning methods, i.e., CNN and spectral-spatial residual network (SSRN) [47].

In PCA, the first three PCs are used as features for data classification. For the conventional SSA, the window size L is selected as 10, and the EVG is fixed to 1. As for the EAP method, it is constructed using threshold values in the range from 2.5% to 10% with respect to the mean of the individual features and with a step of 2.5% for the standard deviation attribute. The thresholds of 200, 500, and 1000 were chosen for the area attribute [48]. The Gabor filtering has three scales and eight orientations, and the 2-D Gabor filters are applied on the first three PCs of the original HSI. With EPF to extract probabilistic features and the SVM classifier for data classification, EPF can improve the classification accuracy in comparison with conventional feature extraction methods, its corresponding parameters, i.e., the filtering size and blur degree are fixed as $\delta s = 3$, $\delta r = 0.2$, $r = 3$, and $\in = 0.01$ as suggested in [49]. With a patch-based architecture, the CNN model in [50] is for the extraction of local spectral-spatial features, followed by a SVM classifier for data classification, thus it is namely CNN-SVM. In the CNN architecture [50], for each pixel, a $9 \times 9 \times B$ 3-D neighborhood is selected and fed into a pretrained network, where B is the number of bands in the HSI. This ends up with a feature vector associated with the central pixel. Because of its similar processing manner to our method, we choose it for comparison. For SSRN, one 3-D convolution and another 2-D convolution are employed to extract the spectral features and spatial features in a cascade manner, respectively, which is also quite similar to the way we adopted. The parameters of SSRN are set according to the original article [47]. In our proposed approach, the parameters include a neighborhood window size of 5×5, $L = 20$, and $S = 15$. In relation to the SVM classifier, the parameters C and γ of the Gaussian kernel are optimally determined via a fivefold cross validation as 1000 and 0.125 for both the Indian Pines and Pavia University datasets, or 100 and 0.125 for the DFC2018 Houston dataset.

Tables IV–VI show that the proposed method obtains the best performance in almost all land-cover classes compared to other similar approaches. In general, PCA has quite poor performance as it is quite noise-sensitive. The conventional SSA improves the classification accuracy on the Indian Pines dataset, yet it achieves a low accuracy on the Pavia University dataset, probably because the reconstructed pixels are excessively smooth so that they are misclassified. The other two methods, EAP and Gabor, achieve good classification accuracy from the derived spectral-spatial features. EPF uses the single scale EPF only can extract limited spatial features, leading to the general classification accuracy. CNN uses a multilayer structure to make full use of local spatial and spectral information and achieve a better accuracy. Not surprisingly, SSRN has the best classification results on all datasets. Our 1.5D-SSA achieves the higher accuracy than all methods except SSRN in most of the land-cover classes, showing a great improvement in HSI classification especially compared with the conventional SSA. In addition, the spectral and local spatial features extracted by our method are comparable and superior to those mined by CNN with a shallow structure.

For the DFC2018 Houston dataset, the classification becomes challenging due to similar urban scenes in the hypercube. First, both PCA and conventional SSA have difficulties in classifying roads and parking lots, where the classification accuracy for these classes is 0. The task of identifying and separating between roads, sidewalks, major thoroughfares proved very difficult, unpaved parking lots and cars are completely missed, even for the CNN base classifier [51]. PCA has less spectral information. And in the first three PCs, the spatial information of some fine or strip-shaped features such as Sidewalks, parking lots and Cars, is very similar to buildings which are over a large area, and it is easy to be misclassified. While SSA retains the trend, but ignores some identifying information in spectral profiles of the ground features. In addition, the limited sample size of some ground features also leads to classification errors. It can be learned that SSA has difficulty in distinguishing similar features. With spatial features used, EAP, Gabor, and EPF have produced improved classification results, though the improvement is still limited. In the deep learning methods, CNN with shallow structures can achieve good but limited results, SSRN achieves the best accuracy due to the high capacity of deep feature extraction. Our proposed method has obtained better classification results compared with conventional methods, especially in effectively distinguishing different impervious surfaces, such as buildings, parking lots, and even cars.

Figs. 5–7 show the visual maps of the classification results obtained by different methods on the three datasets. As seen, the results from the raw data, PCA, and conventional SSA contain many misclassified pixels within the different land-cover

TABLE IV
CLASSIFICATION RESULTS (%) FOR THE INDIAN PINES DATASET

#	Train	Test	SVM	PCA	SSA	EAP	Gabor	EPF	CNN-SVM	SSRN	1.5D-SSA
C1	5	41	14.63	26.83	73.17	**95.12**	80.49	77.78	97.78	94.44	78.05
C2	143	1285	75.33	36.96	81.87	82.88	85.91	95.21	91.35	**96.03**	93.62
C3	83	747	66.67	43.91	77.38	86.75	88.62	83.03	93.36	**98.22**	91.70
C4	24	213	46.01	10.80	70.42	81.69	94.84	99.14	84.91	**95.36**	87.32
C5	49	434	85.71	26.50	94.47	94.93	92.86	88.37	97.46	95.04	**97.47**
C6	73	657	92.39	95.74	92.54	98.63	86.30	78.88	90.49	99.65	**98.78**
C7	3	25	68.00	52.00	80.00	84.00	92.00	**100.00**	96.30	**100.00**	92.00
C8	48	430	99.07	97.44	99.77	99.30	96.05	98.72	**100.00**	**100.00**	99.77
C9	2	18	33.33	11.11	55.56	**100.00**	44.44	52.63	**100.00**	66.67	83.33
C10	98	874	75.06	54.58	84.21	85.35	86.16	87.92	**92.12**	98.45	92.11
C11	246	2209	84.56	82.66	84.93	92.53	91.08	96.51	96.09	95.64	**96.70**
C12	60	533	61.54	9.76	74.30	80.30	86.49	79.52	79.86	**98.59**	87.24
C13	21	184	91.85	93.48	90.76	**98.91**	90.22	73.50	99.00	96.43	**98.91**
C14	127	1138	93.76	97.89	91.39	99.30	93.94	93.38	98.87	**99.71**	98.07
C15	39	347	57.35	11.24	49.57	**98.27**	77.23	87.83	94.71	85.64	90.78
C16	10	83	79.52	95.18	85.54	**100.00**	**100.00**	61.54	95.60	95.83	**100.00**
	OA		79.75	62.64	84.02	91.19	89.25	90.32	93.84	**96.92**	94.89
	AA		70.30	52.88	80.37	92.37	96.66	84.62	94.24	**96.73**	92.87
	Kappa		0.77	0.56	0.82	0.90	0.88	0.89	0.93	**0.96**	0.94

TABLE V
CLASSIFICATION RESULTS (%) FOR THE PAVIA UNIVERSITY DATASET

#	Train	Test	SVM	PCA	SSA	EAP	Gabor	EPF	CNN-SVM	SSRN	1.5D-SSA
C1	664	5967	94.34	91.87	93.88	**99.45**	94.59	93.69	96.53	99.94	99.33
C2	1865	16784	97.98	98.62	97.76	98.30	97.53	99.90	99.11	**100.00**	99.80
C3	210	1889	81.52	35.84	78.30	**98.09**	80.15	85.54	96.50	94.21	95.13
C4	307	2757	95.14	74.46	94.60	93.76	88.21	66.57	96.92	**98.26**	98.08
C5	135	1210	99.50	99.34	99.50	99.59	99.92	**100.00**	**100.00**	99.51	99.59
C6	503	4526	88.42	17.26	76.82	96.58	88.38	98.04	98.16	**100.00**	98.61
C7	133	1197	86.72	0.42	86.55	99.42	76.61	94.26	88.59	**99.58**	97.74
C8	369	3313	88.92	84.58	89.22	98.49	89.13	71.42	85.97	**99.43**	98.22
C9	95	852	**100.00**	99.88	99.88	**100.00**	90.73	66.45	82.99	**100.00**	**100.00**
	OA		94.24	78.99	92.53	98.07	93.03	92.26	97.33	**99.51**	99.03
	AA		92.51	66.92	90.72	98.19	89.47	86.21	93.86	**99.49**	98.50
	Kappa		0.92	0.71	0.90	0.97	0.91	0.90	0.96	0.98	**0.99**

regions. These can be easily found among the adjacent land-cover regions, such as the road and buildings in the DFC2018 Houston dataset. This validates the limited performance when using only the spectral features in the HSI data classification. For EAP and Gabor, the misclassified pixels are greatly reduced, especially for large objects, thanks to the use of the spatial information. However, because of the effect of spatial feature extraction scale, some small land-covers adjacent to large land-cover regions can still be easily misclassified. EPF can further reduce misclassification inside land-covers, while lump or strip misclassification due to single spatial features still exists. For CNN, its patch-based feature extraction manner causes the blurring of the edges, leading to classification errors, while SSRN can well preserve the boundaries of different land-covers. Our method can also effectively solve the above problems in the HSI classification, where various impervious surfaces and vegetation can be correctly distinguished while well preserving the boundary between different land-cover regions.

E. Evaluation Under Different Classifiers

Although the SVM classifier is utilized for the data classification in our experiments, we can certainly use other classifiers for classifying the features extracted by using the proposed 1.5D-SSA model. To verify the efficacy of the extracted features from the proposed model, another two widely used classifiers,

TABLE VI
CLASSIFICATION RESULTS (%) FOR THE DFC2018 HOUSTON DATASET

#	Train	Test	SVM	PCA	SSA	EAP	Gabor	EPF	CNN-SVM	SSRN	1.5D-SSA
C1	81	731	19.32	2.88	11.64	19.32	**44.38**	25.48	22.60	37.12	17.81
C2	1538	13850	54.70	0.45	10.69	54.70	51.55	33.97	55.56	**82.42**	74.10
C3	552	4971	37.32	0.00	0.26	37.32	38.63	53.88	72.15	**85.39**	47.65
C4	114	1032	19.01	0.00	0.00	19.01	75.75	77.98	76.62	**88.07**	44.03
C5	9786	88078	81.13	71.92	73.74	81.13	75.20	79.46	81.09	**84.40**	84.26
C6	6944	62502	70.06	60.33	59.96	70.06	72.36	70.13	73.60	**85.70**	80.69
C7	5228	47054	21.55	0.20	4.14	21.55	38.21	26.17	31.36	**43.50**	36.31
C8	195	1763	4.77	0.00	0.00	4.77	26.90	12.15	10.22	**27.87**	11.75
C9	6291	56619	72.04	22.16	42.98	72.04	59.35	65.62	69.06	**80.01**	74.37
C10	422	3800	72.94	0.00	0.00	72.94	43.70	76.70	65.36	76.84	**90.79**
C11	58	529	38.26	0.00	0.00	38.26	38.07	46.02	57.95	**87.50**	22.54
C12	73	660	56.9	0.00	0.00	56.90	49.92	90.23	92.11	**94.39**	84.07
OA			60.70	40.41	46.27	63.70	62.46	62.37	66.44	**76.35**	71.52
AA			43.57	8.77	11.30	45.67	51.17	54.97	58.97	**72.77**	55.70
Kappa			0.52	0.18	0.27	0.52	0.51	0.50	0.56	**0.69**	0.63

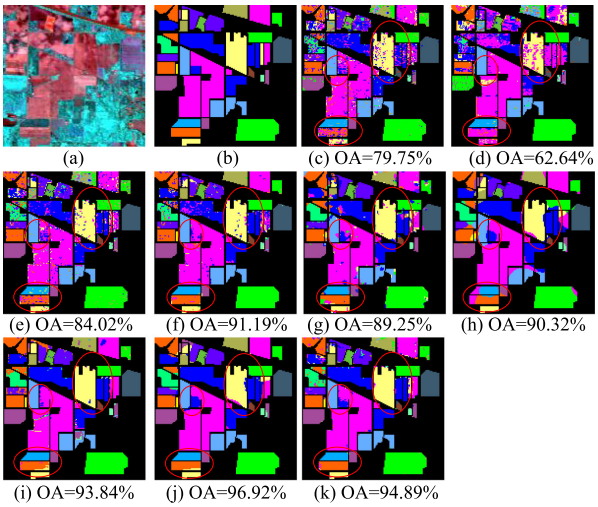

Fig. 5. (a) False color image of Indian Pines. (b) Ground truth image. (c) SVM. (d) PCA. (e) SSA. (f) EAP. (g) Gabor. (h) EPF. (i) CNN-SVM. (j) SSRN. (k) 1.5D-SSA.

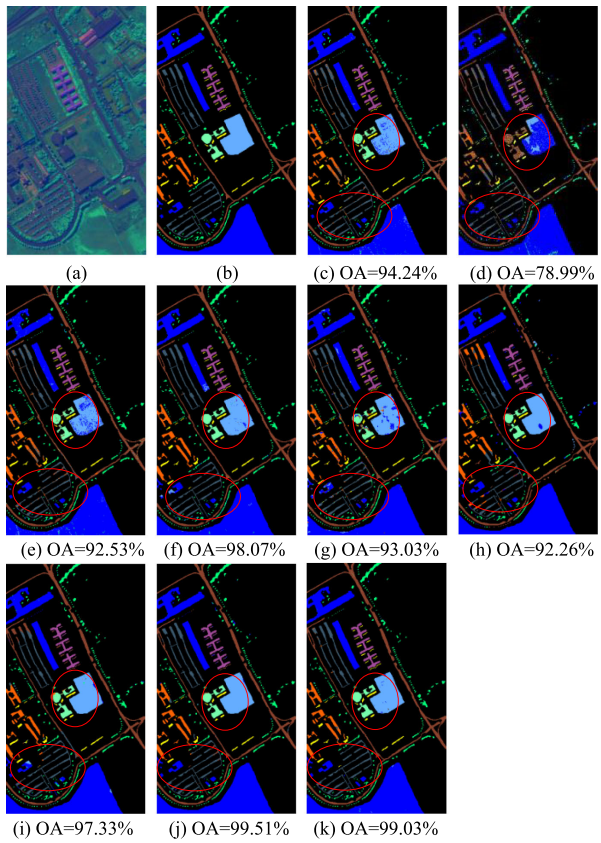

Fig. 6. (a) False color image of Pavia University. (b) Ground truth image. (c) SVM. (d) PCA. (e) SSA. (f) EAP. (g) Gabor. (h) EPF. (i) CNN-SVM. (j) SSRN. (k) 1.5D-SSA.

the multinomial logistic regression (MLR) [52] and sparse representation classifier (SRC) [53] are also used for comparison. With default parameter settings as suggested in [52] and [53], the classification results from these two classifiers and SVM are produced for comparison, where three types of features are used, including the raw data, CNN features (i.e., the spectral-spatial features in the CNN-SVM method), and our proposed 1.5D-SSA features. The results from the three datasets are summarized in Table VII for comparison.

As seen in Table VII, in comparison to the raw data in HSI, the extracted 1.5D-SSA features have significantly improved the classification accuracy with all the three classifiers, in which the 1.5D-SSA features seem to be superior than the CNN features. As for different classifiers, the results from the MLR and SRC are inferior to those from the SVM, which indicates the strong capacity of the SVM with the RBF kernel in classifying the HSI data. For a weak classifier such as MLR, the classification accuracy has been improved with the largest scale when the raw data are replaced by the 1.5D-SSA features. Specifically, the OA has increased by about 25% for Indian Pines, 10% for Pavia University, and 15% for the DEC2018 datasets. In

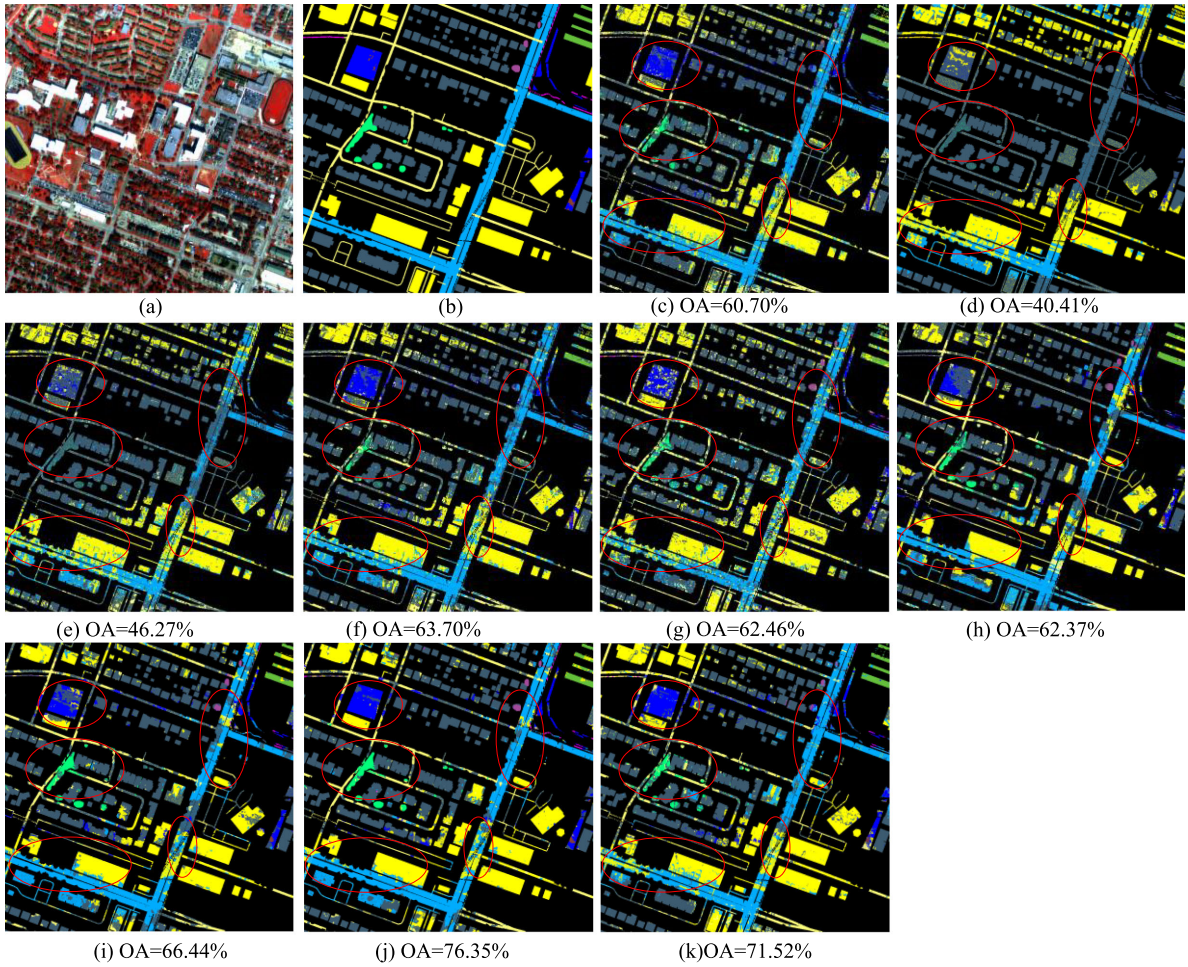

Fig. 7. (a) False color image of DFC2018 Houston. (b) Ground truth image. (c) SVM. (d) PCA. (e) SSA. (f) EAP. (g) Gabor. (h) EPF. (i) CNN-SVM. (j) SSRN. (k) 1.5D-SSA.

TABLE VII
CLASSIFICATION RESULTS (%) WITH DIFFERENT FEATURES USING THE MLR, SRC, AND SVM CLASSIFIERS ON THE THREE DATASETS (ABOUT 10% TRAINING SAMPLES PER CLASS)

Datasets	Metrics	Raw			CNN features			1.5D-SSA features		
		MLR	SRC	SVM	MLR	SRC	SVM	MLR	SRC	SVM
Indian Pines	OA	65.58	63.96	72.41	71.29	82.17	88.24	91.72	84.10	**91.76**
	AA	63.62	70.03	82.07	79.33	89.61	93.95	93.39	91.29	**95.41**
	Kappa	0.60	0.59	0.69	0.67	0.80	0.87	0.90	0.80	**0.91**
Pavia University	OA	75.14	74.51	88.29	80.20	85.03	90.94	85.68	88.30	**95.52**
	AA	73.80	79.76	90.57	81.70	86.31	94.26	82.57	91.80	**96.91**
	Kappa	0.66	0.67	0.85	0.74	0.83	0.88	0.81	0.84	**0.94**
DFC2018 Houston	OA	30.62	49.43	54.15	48.19	53.86	57.46	45.57	52.48	**62.75**
	AA	39.66	64.03	69.38	54.35	71.41	**78.18**	58.87	68.03	71.74
	Kappa	0.19	0.39	0.44	0.36	0.44	0.48	0.34	0.42	**0.63**

addition, the improvement of OA on SRC from raw data to the proposed 1.5D-SSA features is also higher than the SVM classifier. Considering the limited generalization capacity of these two classifiers, the significant improvements of OA can be mainly attributed to the enhanced discrimination ability of the extracted 1.5D-SSA features.

F. Simulation Analysis of Near Real Time

Compared with conventional SSA, the offline computation time (running time for performing the feature extraction after acquisition) of 1.5D-SSA is obviously longer on account of the extraction of local spatial information. However, the proposed

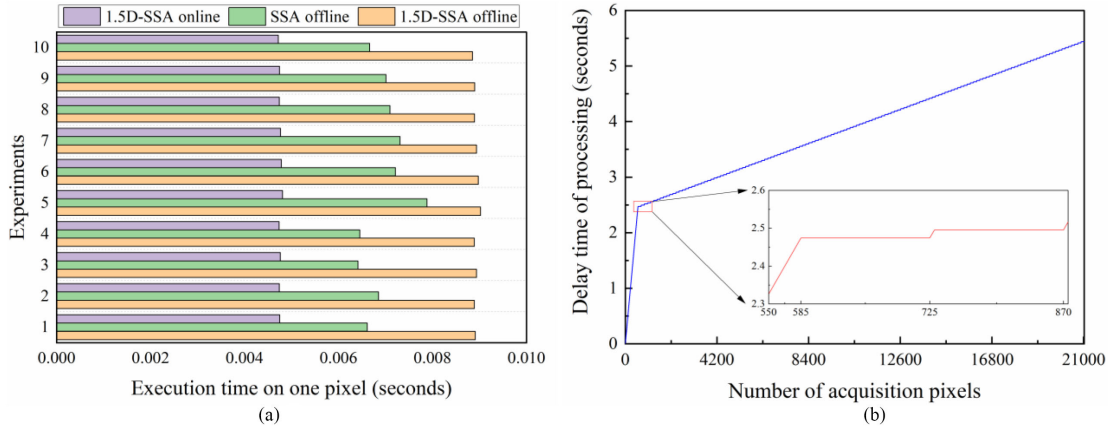

Fig. 8. (a) Comparison of execution time on one pixel between 1.5D-SSA online time, SSA, and 1.5D-SSA offline time. (b) Delay time of pixel processing compared with pixel acquisition.

near real-time procedure is an online processing form, which can be expected to save the time cost of postprocessing.

First, we compare the time cost of offline processing with online processing, taking the whisk-broom scanning as an example. Assuming that the time for collecting one pixel of the hyperspectral device and processing on one pixel of 1.5D-SSA are t_1 and t_2, respectively, and the size of HSI image is $m \times n$. The offline computation time is T_1

$$T_1 = (m \times n) \cdot (t_1 + t_2). \tag{2}$$

While for the online computation time T_2 as follows:

$$T_2 = \begin{cases} (m \times n) \cdot t_1 + (m-w+1) \times (n-w+1) \cdot (t_2 - t_1), & t_2 > t_1 \\ (m \times n) \cdot t_1 + [m \times n - (m-w) \times (n-w)] \cdot t_2, & t_2 = t_1 \\ (m \times n) \cdot t_1, & t_2 < t_1 \end{cases} \tag{3}$$

where w is the window size. In (3), we give three calculations of T_2, considering the difference in t_1 and t_2. Obviously, the time T_2 for the near real-time procedure is smaller than postprocessing time T_1.

Take $t_1 = t_2$ as an example, results from two simulation experiments based on the Indian Pines dataset are given in Fig. 8, which shows a comparison of the online and offline time in processing one pixel, as well as the delay time in comparison to data acquisition. Fig. 8(a) shows the execution time on one pixel of three processing: SSA offline, 1.5D-SSA offline, and 1.5D-SSA online (average time per pixel based on T_2) for each of ten experiments. As can be seen, the proposed near real-time method can save the computation time and improve processing efficiency compared to offline method.

In addition, the delay time of pixel processing compared with pixel acquisition is shown in Fig. 8(b). The delay time increases linearly in the stage that captured pixels cannot form a neighborhood, due to the pixels are only collected without processing. After 1.5D-SSA starts processing, the delay time increases slowly: 1) the delay time remains the same for a short period of time (such as red line from 585 to 725 pixels in expanded graph), because the acquisition and processing of a certain number of pixels (140 in this experiment) are simultaneous; 2) a small linear time increase (such as in 725 and 870 pixels in expanded graph) occurs when collecting the next row of pixels, as the first w (5 in this experiment) pixels on next row take time to be collected to form a neighborhood. As shown in Fig. 8(b), the overall delay time is 5.41 s for a size of 145 $\times$ 145 $\times$ 200 HSI data. There is no doubt that the proposed method is near real time.

V. Conclusion

In the domain of image processing and machine vision, feature extraction is one of the important research, especially for the HSI in remote sensing. Comprehensive utilization of spectral and spatial information is essential for feature extraction in HSI.

Conventional SSA has shown good performance for feature extraction and denoising in the HSI data. Based on SSA, a novel 1.5D-SSA method is proposed, which can exploit not only the spectral content but also local spatial information in this article. In order to exploit the spatial content, a small neighborhood is chosen for each pixel, and a given number of similar pixels are rearranged together into an extended vector, where SSA is applied. By this implementation, visual inspection of the reconstructed pixels seems to indicate that they are able to preserve detailed features. Moreover, based on two of the most common acquisition paradigms in HSI devices: pixel and line scanning, a near real-time implementation strategy is further developed, meeting the requirement of online image analysis and reducing the higher computation time.

Classification results on two benchmark datasets and one actual dataset show that the proposed method has a higher classification accuracy, using the SVM classifier for performance evaluation. Meanwhile, the simulated analysis and results demonstrate that the near real-time strategy improves efficacy in feature extraction.

In addition, considering that the KWE and the KCE have good performance for texture recognition and image segmentation in the synthetic aperture radar (SAR), these can be investigated in the future for more effective feature extraction and data classification in HSI.

ACKNOWLEDGMENT

The authors would like to thank the IEEE GRSS IADF and the Hyperspectral Image Analysis Lab at the University of Houston for providing the DFC2018 Houston hyperspectral dataset, and this dataset is obtained from http://hyperspectral.ee.uh.edu/?page_id=1075.

REFERENCES

[1] M. Esnaashari and M. R. Meybodi, "Irregular cellular learning automata," *IEEE Trans. Cybern.*, vol. 45, no. 8, pp. 1622–1632, Aug. 2015.

[2] B. Debnath, J. C. Das, and D. De, "Reversible logic-based image steganography using quantum dot cellular automata for secure nanocommunication," *IET Circuits, Devices Syst.*, vol. 11, no. 1, pp. 58–67, 2017.

[3] M. Li, D. Lu, W. Wen, H. Ren, and Y. Zhang, "Cryptanalyzing a color image encryption scheme based on hybrid hyper-chaotic system and cellular automata," *IEEE Access*, vol. 6, pp. 47102–47111, 2018.

[4] H. Ramezani, H. ZakiDizaji, H. Masoudi, and G. Akbarizadeh, "A new DSWTS algorithm for real-time pedestrian detection in autonomous agricultural tractors as a computer vision system," *Measurement*, vol. 93, pp. 126–134, 2016.

[5] G. Akbarizadeh, "A new statistical-based kurtosis wavelet energy feature for texture recognition of SAR images," *IEEE Trans. Geosci. Remote Sens.*, vol. 50, no. 11, pp. 4358–4368, Nov. 2012.

[6] Z. Tirandaz and G. Akbarizadeh, "A two-phase algorithm based on kurtosis curvelet energy and unsupervised spectral regression for segmentation of SAR Images," *IEEE J. Sel. Topics Appl. Earth Observ. Remote Sens.*, vol. 9, no. 3, pp. 1244–1264, Mar. 2016.

[7] Z. Liu, F. Li, N. Li, R. Wang, and H. Zhang, "A novel region-merging approach for coastline extraction from sentinel-1A IW mode SAR imagery," *IEEE Geosci. Remote Sens. Lett.*, vol. 13, no. 3, pp. 324–328, Mar. 2016.

[8] Z. Zhu, Y. Tang, J. Hu, and M. An, "Coastline extraction from high-resolution multispectral images by integrating prior edge information with active contour model," *IEEE J. Sel. Topics Appl. Earth Observ. Remote Sens.*, vol. 12, no. 10, pp. 4099–4109, Oct. 2019.

[9] Z. Tirandaz, G. Akbarizadeh, and H. Kaabi, "PolSAR image segmentation based on feature extraction and data compression using weighted neighborhood filter bank and hidden Markov random field-expectation maximization," *Measurement*, vol. 153, 2020, Art. no. 107432.

[10] R. Green *et al.*, "Imaging spectroscopy and the airborne visible/Infrared imaging spectrometer (AVIRIS)," *Remote Sens. Environ.*, vol. 65, pp. 227–248, 1998.

[11] J. Zabalza *et al.*, "Novel Folded-PCA for improved feature extraction and data reduction with hyperspectral imaging and SAR in remote sensing," *ISPRS J. Photogrammetry Remote Sens.*, vol. 93, pp. 112–122, 2014.

[12] T. Qiao *et al.*, "Effective denoising and classification of hyperspectral images using curvelet transform and singular spectrum analysis," *IEEE Trans. Geosci. Remote Sens.*, vol. 55, no. 1, pp. 119–133, Jan. 2017.

[13] G. Chen and S.-E. Qian, "Denoising of hyperspectral imagery using principal component analysis and wavelet shrinkage," *IEEE Trans. Geosci. Remote Sens.*, vol. 49, no. 3, pp. 973–980, Mar. 2011.

[14] T. Qiao *et al.*, "Joint bilateral filtering and spectral similarity-based sparse representation: A generic framework for effective feature extraction and data classification in hyperspectral imaging," *Pattern Recognit.*, vol. 77, pp. 316–328, 2018.

[15] X. Kang, X. Xiang, S. Li, and J. A. Benediktsson, "PCA-based edge-preserving features for hyperspectral image classification," *IEEE Trans. Geosci. Remote Sens.*, vol. 55, no. 12, pp. 7140–7151, Dec. 2017.

[16] J. Zabalza, R. Jinchang, W. Zheng, S. Marshall, and W. Jun, "Singular spectrum analysis for effective feature extraction in hyperspectral imaging," *IEEE Geosci. Remote Sens. Lett.*, vol. 11, no. 11, pp. 1886–1890, Nov. 2014.

[17] J. Zabalza, J. Ren, Z. Wang, H. Zhao, J. Wang, and S. Marshall, "Fast implementation of singular spectrum analysis for effective feature extraction in hyperspectral imaging," *IEEE J. Sel. Topics Appl. Earth Observ. Remote Sens.*, vol. 8, no. 6, pp. 2845–2853, Jun. 2015.

[18] P. R. Marpu, M. Pedergnana, M. D. Mura, J. A. Benediktsson, and L. Bruzzone, "Automatic generation of standard deviation attribute profiles for spectral–spatial classification of remote sensing data," *IEEE Geosci. Remote Sens. Lett.*, vol. 10, no. 2, pp. 293–297, Mar. 2013.

[19] S. Jia, L. Shen, and Q. Li, "Gabor feature-based collaborative representation for hyperspectral imagery classification," *IEEE Trans. Geosci. Remote Sens.*, vol. 53, no. 2, pp. 1118–1129, Feb. 2015.

[20] J. Zabalza *et al.*, "Novel two-dimensional singular spectrum analysis for effective feature extraction and data classification in hyperspectral imaging," *IEEE Trans. Geosci. Remote Sens.*, vol. 53, no. 8, pp. 4418–4433, Aug. 2015.

[21] J. Zabalza, C. Qing, P. Yuen, G. Sun, H. Zhao, and J. Ren, "Fast implementation of two-dimensional singular spectrum analysis for effective data classification in hyperspectral imaging," *J. Franklin Inst.*, vol. 355, no. 4, pp. 1733–1751, 2018.

[22] J. Xia, L. Bombrun, T. Adalı, Y. Berthoumieu, and C. Germain, "Spectral–spatial classification of hyperspectral images using ICA and edge-preserving filter via an ensemble strategy," *IEEE Trans. Geosci. Remote Sens.*, vol. 54, no. 8, pp. 4971–4982, Aug. 2016.

[23] X. Kang, S. Li, L. Fang, and J. A. Benediktsson, "Intrinsic image decomposition for feature extraction of hyperspectral images," *IEEE Trans. Geosci. Remote Sens.*, vol. 53, no. 4, pp. 2241–2253, Apr. 2015.

[24] B. Sun, X. Kang, S. Li, and J. A. Benediktsson, "Random-walker-based collaborative learning for hyperspectral image classification," *IEEE Trans. Geosci. Remote Sens.*, vol. 55, no. 1, pp. 212–222, Jan. 2017.

[25] F. Samadi, G. Akbarizadeh, and H. Kaabi, "Change detection in SAR images using deep belief network: A new training approach based on morphological images," *IET Image Process.*, vol. 13, no. 12, pp. 2255–2264, 2019.

[26] F. Sharifzadeh, G. Akbarizadeh, and Y. Seifi Kavian, "Ship classification in SAR images using a new hybrid CNN–MLP classifier," *J. Indian Soc. Remote Sens.*, vol. 47, no. 4, pp. 551–562, 2018.

[27] Y. Chen, Y. Wang, Y. Gu, X. He, P. Ghamisi, and X. Jia, "Deep learning ensemble for hyperspectral image classification," *IEEE J. Sel. Topics Appl. Earth Observ. Remote Sens.*, vol. 12, no. 6, pp. 1882–1897, Jun. 2019.

[28] O. Oktay *et al.*, "Anatomically constrained neural networks (ACNNs): Application to cardiac image enhancement and segmentation," *IEEE Trans. Med. Imag.*, vol. 37, no. 2, pp. 384–395, Feb. 2018.

[29] M. Zalpour, G. Akbarizadeh, and N. Alaei-Sheini, "A new approach for oil tank detection using deep learning features with control false alarm rate in high-resolution satellite imagery," *Int. J. Remote Sens.*, vol. 41, no. 6, pp. 2239–2262, 2019.

[30] X. Kang, C. Li, S. Li, and H. Lin, "Classification of hyperspectral images by gabor filtering based deep network," *IEEE J. Sel. Topics Appl. Earth Observ. Remote Sens.*, vol. 11, no. 4, pp. 1166–1178, Apr. 2018.

[31] Y. Guo, H. Cao, J. Bai, and Y. Bai, "High efficient deep feature extraction and classification of spectral-spatial hyperspectral image using cross domain convolutional neural networks," *IEEE J. Sel. Topics Appl. Earth Observ. Remote Sens.*, vol. 12, no. 1, pp. 345–356, Jun. 2019.

[32] Y. Kong, X. Wang, and Y. Cheng, "Spectral–spatial feature extraction for HSI classification based on supervised hypergraph and sample expanded CNN," *IEEE J. Sel. Topics Appl. Earth Observ. Remote Sens.*, vol. 11, no. 11, pp. 4128–4140, Nov. 2018.

[33] E. Aptoula, M. C. Ozdemir, and B. Yanikoglu, "Deep learning with attribute profiles for hyperspectral image classification," *IEEE Geosci. Remote Sens. Lett.*, vol. 13, no. 12, pp. 1970–1974, Dec. 2016.

[34] L. Heming and Q. Li, "Hyperspectral imagery classification using sparse representations of convolutional neural network features," *Remote Sens.*, vol. 8, 2016, Art. no. 99.

[35] J. Zabalza, J. Ren, J. Ren, Z. Liu, and S. Marshall, "Structured covariance principal component analysis for real-time onsite feature extraction and dimensionality reduction in hyperspectral imaging," *Appl. Opt.*, vol. 53, no. 20, pp. 4440–4449, Jul. 2014.

[36] S. Sanchez, G. Martín, A. Paz, A. Plaza, and J. Plaza, "Near real-time endmember extraction from remotely sensed hyperspectral data using NVidia GPUs," *Proc. SPIE*, vol. 7724, 2010, Art. no. 772409.

[37] W. Yang, L. Gao, and D. Chen, "Real-time target detection in hyperspectral images based on spatial-spectral information extraction," *EURASIP J. Adv. Signal Process.*, vol. 2012, 2012, Art. no. 142.

[38] P. Horstrand, M. Díaz, R. Guerra, S. López, and J. F. López, "A novel hyperspectral anomaly detection algorithm for real-time applications with push-broom sensors," *IEEE J. Sel. Topics Appl. Earth Observ. Remote Sens.*, vol. 12, no. 12, pp. 4787–4797, Dec. 2019.

[39] M. Díaz *et al.*, "Real-time hyperspectral image compression onto embedded GPUs," *IEEE J. Sel. Topics Appl. Earth Observ. Remote Sens.*, vol. 12, no. 8, pp. 2792–2809, Aug. 2019.

[40] F. Vagni, "Survey of Hyperspectral and Multispectral Imaging Technologies (Etude sur les technologies d'imagerie hyperspectrale et multispectrale)," p. 44, 2007.

[41] J. Zabalza, T. Qiao, and S. Marshall, "On the fly' dimensionality reduction for hyperspectral image acquisition," in *Proc. 23rd Eur. Signal Process. Conf.*, Nice, France, 2015, pp. 749–753.

[42] N. Golyandina and A. Zhigljavsky, *Singular Spectrum Analysis for Time Series (SpringerBriefs in Statistics)*. Berlin, Germany: Springer Science, 2013.
[43] G. Hughes, "On the mean accuracy of statistical pattern recognizers," *IEEE Trans. Inf. Theory*, vol. 14, no. 1, pp. 55–63, Jan. 1968.
[44] R. Archibald and G. Fann, "Feature selection and classification of hyperspectral images with support vector machines," *IEEE Geosci. Remote Sens. Lett.*, vol. 4, no. 4, pp. 674–677, Oct. 2007.
[45] C. Chih-Chung and L. Chih-Jen, "LIBSVM: A library for support vector machines," *ACM Trans. Intell. Syst. Technol.*, vol. 2, no. 3, pp. 1–27, 2011.
[46] H. Zhang, J. Li, Y. Huang, and L. Zhang, "A nonlocal weighted joint sparse representation classification method for hyperspectral imagery," *IEEE J. Sel. Topics Appl. Earth Observ. Remote Sens.*, vol. 7, no. 6, pp. 2056–2065, Jun. 2014.
[47] Z. Zhong, J. Li, Z. Luo, and M. Chapman, "Spectral–spatial residual network for hyperspectral image classification: A 3-D deep learning framework," *IEEE Trans. Geosci. Remote Sens.*, vol. 56, no. 2, pp. 847–858, Feb. 2018.
[48] J. Li *et al.*, "Multiple feature learning for hyperspectral image classification," *IEEE Trans. Geosci. Remote Sens.*, vol. 53, no. 3, pp. 1592–1606, Mar. 2015.
[49] X. Kang, S. Li, and J. A. Benediktsson, "Spectral–spatial hyperspectral image classification with edge-preserving filtering," *IEEE Trans. Geosci. Remote Sens.*, vol. 52, no. 5, pp. 2666–2677, May 2014.
[50] B. Liu, X. Yu, P. Zhang, A. Yu, Q. Fu, and X. Wei, "Supervised deep feature extraction for hyperspectral image classification," *IEEE Trans. Geosci. Remote Sens.*, vol. 56, no. 4, pp. 1909–1921, Apr. 2018.
[51] Y. Xu *et al.*, "Advanced multi-sensor optical remote sensing for urban land use and land cover classification: Outcome of the 2018 IEEE GRSS data fusion contest," *IEEE J. Sel. Topics Appl. Earth Observ. Remote Sens.*, vol. 12, no. 6, pp. 1709–1724, Jun. 2019.
[52] J. Li, J. M. Bioucas-Dias, and A. Plaza, "Spectral–spatial hyperspectral image segmentation using subspace multinomial logistic regression and markov random fields," *IEEE Trans. Geosci. Remote Sens.*, vol. 50, no. 3, pp. 809–823, Mar. 2012.
[53] Y. Chen, N. M. Nasrabadi, and T. D. Tran, "Hyperspectral image classification using dictionary-based sparse representation," *IEEE Trans. Geosci. Remote Sens.*, vol. 49, no. 10, pp. 3973–3985, Oct. 2011.

Hang Fu received the B.Sc. degree from China University of Petroleum (East China), Qingdao, China, in 2019. He is currently working toward the M.Sc. degree in geomatics engineering with the China University of Petroleum (East China), Qingdao, China.

His research interests are related to hyperspectral image feature extraction and classification.

Genyun Sun (Member, IEEE) received the B.S. degree from Wuhan University, Wuhan, China, in 2003, and the Ph.D. degree from the Institute of Remote Sensing Applications, Chinese Academy of Sciences, Beijing, China, in 2008.

He is currently an Associate Professor with the China University of Petroleum, Qingdao, China. His current research interests include remote sensing image processing, hyperspectral remote sensing, high-resolution remote sensing, and intelligent optimization algorithm.

Jaime Zabalza (Member, IEEE) received the M.Eng. degree in industrial engineering from Universitat Jaume I (UJI), Castellón de la Plana, Spain, in 2006, the MAS degree in electrical technology from the Universitat Politècnica de València, València, Spain, in 2010, and the M.Sc. degree (with distinction) in electronic and electrical engineering and the Ph.D. degree in hyperspectral imaging from the University of Strathclyde, Glasgow, U.K., in 2012 and 2015, respectively.

From 2006 to 2011, he joined UJI as an R&D Engineer and worked with the Energy Technological Institute, Spain, in multidisciplinary fields comprising power electronics, automation, and computer science. He is currently with the Department of Electronic and Electrical Engineering, University of Strathclyde. His research interests include synthetic aperture radar and remote sensing, hyperspectral imaging, and digital signal processing, including signal processing in a wide range of applications.

Aizhu Zhang (Member, IEEE) received the B.Sc., M.Sc., and Ph.D. degrees from China University of Petroleum (East China), Qingdao, China, in 2011, 2014, and 2017, respectively.

She is currently a Lecturer with China University of Petroleum (East China), Qingdao, China. Her research interests include in artificial intelligence, pattern recognition, city remote sensing, and wetland remote sensing.

Jinchang Ren (Senior Member, IEEE) received the Ph.D. degree in electronic imaging and media communication from Bradford University, Bradford, U.K., in 2009.

He is currently a Reader with the Centre for Excellence for Signal and Image Processing, and the Deputy Director of the Strathclyde Hyperspectral Imaging Centre, University of Strathclyde, Glasgow, U.K. His current research interests include visual computing and multimedia signal processing, especially on semantic content extraction for video analysis and understanding and more recently hyperspectral imaging.

Xiuping Jia (Senior Member, IEEE) received the Ph.D. degree in electrical engineering from the University of New South Wales, Sydney, NSW, Australia, in 1996.

She has been with the School of Information Technology and Electrical Engineering, University of New South Wales at Canberra, Canberra, ACT, Australia, since 1988, where she is currently a Senior Lecturer. She is also a Guest Professor with Harbin Engineering University, Harbin, China, and an Adjunct Researcher with the China National Engineering Research Center for Information Technology in Agriculture, Beijing, China. She has co-authored the remote sensing textbook entitled *Remote Sensing Digital Image Analysis* (Springer-Verlag, 3rd ed., 1999 and 4th ed., 2006). Her current research interests include remote sensing and imaging spectrometry.

Dr. Jia is an Editor of the Annals of *GIS* and an Associate Editor of the IEEE TRANSACTIONS ON GEOSCIENCE AND REMOTE SENSING.